High Q and sub-wavelength THz electric field confinement in ultrastrongly coupled THz resonators

Simon Messelot, Solen Coeymans, Jérôme Tignon, Sukhdeep Dhillon, Juliette Mangeney

Research Article Vol. 11, No. 7 / July 2023 / Photonics Research 1203

PHOTONICS Research

High Q and sub-wavelength THz electric field confinement in ultrastrongly coupled THz resonators

Simon Messelot, Solen Coeymans, Jérôme Tignon, Sukhdeep Dhillon, and Juliette Mangeney*

Laboratoire de Physique de l'Ecole Normale Supérieure, Ecole normale supérieure, PSL University, Sorbonne Université, Université Paris Diderot, Sorbonne Paris Cité, CNRS, 24 rue Lhomond, 75005 Paris, France
**Corresponding author: juliette.mangeney@phys.ens.fr*

Received 29 November 2022; revised 16 April 2023; accepted 2 May 2023; posted 4 May 2023 (Doc. ID 482195); published 19 June 2023

The control of light–matter coupling at the single electron level is currently a subject of growing interest for the development of novel quantum devices and for studies and applications of quantum electrodynamics. In the terahertz (THz) spectral range, this raises the particular and difficult challenge of building electromagnetic resonators that can conciliate low mode volume and high quality factor. Here, we report on hybrid THz cavities based on ultrastrong coupling between a Tamm cavity and an LC circuit metamaterial and show that they can combine high quality factors of up to $Q = 37$ with a deep-subwavelength mode volume of $V = 3.2 \times 10^{-4}\lambda^3$. Our theoretical and experimental analysis of the coupled mode properties reveals that, in general, the ultrastrong coupling between a metamaterial and a Fabry–Perot cavity is an effective tool to almost completely suppress radiative losses and, thus, ultimately limit the total losses to the losses in the metallic layer. These Tamm cavity-LC metamaterial coupled resonators open a route toward the development of single photon THz emitters and detectors and to the exploration of ultrastrong THz light–matter coupling with a high degree of coherence in the few to single electron limit.

https://doi.org/10.1364/PRJ.482195

1. INTRODUCTION

The control of light–matter coupling by embedding matter into a photonic resonator is an essential ingredient for the development of single photon devices and cavity quantum electrodynamic studies and applications. The two parameters of photonic resonators that play a key role in light–matter coupling are the quality factor Q, which is inversely proportional to the photon decay rate of the cavity, and the mode volume V, which quantifies the confinement of the electric field. In many cases, photonic resonators associating strong electric field confinement and a high Q are highly desired. For instance, in the weak-coupling regime, the intensity of light–matter interaction is enhanced by the ratio Q/V, as described by Purcell effect [1]. Also, as the light–matter coupling constant g scales with $\sqrt{N_e/V}$, with N_e the number of emitters in the matter part collectively involved in the interaction [2–4], small V are needed to reach the ultrastrong and deep-strong coupling regimes at the single electron level [5–9]. Moreover, the in-depth study of the ultrastrong coupling regime requires a high degree of coherence of the light–matter coupling [10–14], quantified by the cooperativity $C = 4g^2Q/(\omega_0\gamma)$, with γ being the matter non-radiative decay rate and ω_0 being the photonic mode angular frequency, which implies a high Q. Therefore, a current challenge in the development of the light–matter coupling platform is to build photonic resonators that conciliate a small V with a high Q.

The ultrastrong coupling regime in high cooperativity systems has been recently studied using cyclotron resonances in a high-mobility two-dimensional electron gas coupled to various types of terahertz (THz) photonic resonators [15]. For example, using a high-Q THz Fabry–Perot cavity made of distributed Bragg reflectors (DBRs; $Q > 180$), Zhang *et al.* reported $g/\omega_0 \sim 0.1$ with $C > 300$ and showed that these unique conditions increase cyclotron resonance lifetime via the suppression of superradiant decay [16]. More recently, in a similar THz Fabry–Perot cavity, Li *et al.* reported $g/\omega_0 \sim 0.36$ with a record-high cooperativity $C = 3513$, allowing the observation of a vacuum Bloch–Siegert shift in ultra-narrow Landau polaritons [17]. Also, Mavrona *et al.* demonstrated a cooperativity of $C = 57$ and $g/\omega_0 \sim 0.175$ using a Fabry–Perot cavity based on weakly transmitting hole patterned metal layer [18].

However, in these works based on high-Q Fabry–Perot cavities, the light–matter coupling involves a very large number of electrons N_e due to the large V, limited by diffraction to the order of $(\frac{\lambda}{2})^3$. A current challenge to explore advanced quantum phenomena such as the fermionic Rabi model for coupled

systems is to reduce the number of electrons involved in the collective interaction while keeping a high coherence in the system. To this end, using a single complementary LC circuit THz resonator, Rajabali *et al.* recently achieved $g/\omega_0 \sim 0.33$ with $C = 94$ implying an estimated optically active electron number of only 30,000, and even of 2000 with $C = 14$ [19]. Such a small number of electrons are obtained thanks to the confinement in truly all space dimensions of the electromagnetic mode, which leads to a deep sub-wavelength mode volume V, the cooperativity remaining nevertheless moderate due to the low Q factor typical of LC circuit resonators ($Q = 11$).

Potential candidates that have recently emerged to simultaneously achieve a high Q and a strong electric field confinement are hybrid THz resonators based on Fabry–Perot cavities strongly coupled to LC circuit metamaterials. In these hybrid resonators, the strength of the coupling is given by the resonator-to-resonator coupling constant G defined by analogy to the light–matter coupling constant g. The ultrastrong coupling between a THz LC circuit resonator and a THz Fabry–Perot cavity was first reported by Meng *et al.* [20]. The authors demonstrated nonlocal collective interaction of spatially separated metamaterial layers mediated by the cavity photons [20] and also the potential of these hybrid THz resonators for phase-sensitive THz detection of chemical and biological materials [21]. More recently, they have demonstrated ultrastrong coupling between the effective magnetic dipole moments of metallic complementary metasurfaces and the magnetic field of a cavity mode [22]. Also, Jeanin *et al.* reported an hybrid THz cavity based on the coupling between LC circuit resonators and a dipolar antenna to engineer the radiative coupling properties and reach unity absorption [23].

Here, we report on hybrid resonators based on the coupling between a THz Tamm cavity and a THz LC circuit metamaterial. The LC circuit resonators are directly patterned on the metallic mirror of the Tamm cavity and are designed to concentrate the THz electric field. Using transmittance measurements and temporal coupled mode theory, we analyze the properties of the coupled modes and demonstrate the reduced coupling constant $G/\omega_0 \sim 0.1$, showing that the two resonators are in the ultrastrong coupling regime. We further describe how the properties of the coupled modes emerge from the properties of the uncoupled metamaterial and the Fabry–Perot resonators. We show high quality factors, $Q = 37$, explained by the quasi-total suppression of the radiative losses provided by the Tamm cavity and small V, in the $(2–3) \times 10^{-4}\lambda^3$ range, resulting from the principal quality of LC metamaterials. Our study demonstrates that, by combining high Q and small V, Tamm cavity-LC metamaterial coupled cavities fulfill the challenging requirement to conciliate strong THz electric field confinement with high quality factor, which is promising for the exploration of ultrastrong THz light–matter coupling with a high degree of coherence in the limit of a few electrons and for the realization of single photon THz emitters and detectors.

2. STRONG COUPLING BETWEEN TAMM CAVITIES AND LC METAMATERIALS

Our dual-cavity THz resonator is based on a hybrid THz Tamm cavity and an LC metamaterial structure and is presented in Fig. 1(a). The Tamm cavity [24,25], on its own, consists of a DBR composed of two high-resistivity silicon wafers of thickness 66 μm ($\sim \frac{3\lambda}{4}$) separated by a vacuum layer of thickness 75 μm ($\sim \frac{\lambda}{4}$) and a 100-nm-thick metallic gold mirror deposited on the top silicon wafer of the DBR [26]. The calculated reflection spectrum of this Tamm cavity, obtained by the finite element method (FEM, COMSOL Multiphysics), exhibits a Tamm mode at 0.98 THz and a resonance linewidth of $\Gamma_{\text{Tamm}} = 0.098$ THz, which gives a quality factor $Q = 100$ [see Fig. 1(b)]. The isolated LC metamaterial, whose base unit cell is presented in Fig. 1(a), is basically a gold layer including patterned holes giving its resonance properties. This pattern should not be mistaken for a complementary split ring resonator that is efficient for concentrating the magnetic field. The model we present concentrates the electric field at its center, similar to conventional split ring resonator, which is crucial for coupling it to matter systems involving the electric dipole interaction, such as in the common two-dimensional electron gas. For this reason, we call this pattern grid split ring resonators (GSRRs). The calculated transmission spectrum of an isolated GSRR metamaterial of dimensions $w = 4.4$ μm, $l = 4.4$ μm, and $L = 16.5$ μm, shows an LC metamaterial resonant mode at 1 THz with a linewidth $\Gamma_{\text{LC}} = 0.222$ THz, resulting in a quality factor $Q = 4.5$ [see Fig. 1(b)]. The hybrid THz resonator structures were fabricated by manually stacking commercially available thin silicon wafers

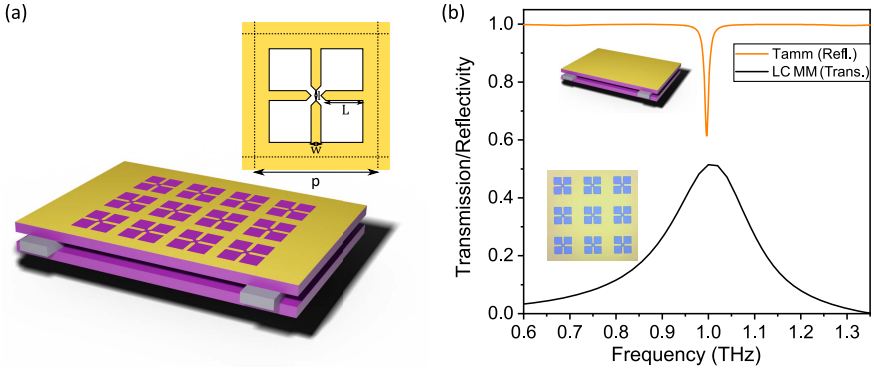

Fig. 1. (a) Representation of the Tamm cavity/LC metamaterial coupled resonators structure and unit cell pattern of the LC metamaterial. (b) Reflection and transmission spectra of the uncoupled Tamm cavity and LC metamaterial, respectively, alongside their representations (inset).

and precision machined thin metal strips opening vacuum gaps, creating the THz DBR. The stacking is realized in a custom-made sample holder dedicated to maintaining the metal spacers positions and holding the stack together by applying pressure. Prior to stacking, the LC metamaterials were patterned on the top silicon wafer by performing a simple optical lithography and the deposition of a 3/100 nm chromium/gold metallic mirror via thermal evaporation under vacuum, followed by a lift-off.

We fabricated nine different Tamm cavity-LC metamaterial coupled resonators, tuning the uncoupled resonance frequencies of the LC metamaterial f_{LC} by applying an homothetic transformation to the w, l, and L dimensions of the LC circuit resonator at a fixed metamaterial period $p = 65$ μm. We probe their optical properties in a transmission experiment using a Bruker Vertex 70v FTIR under vacuum, a Globar blackbody source, and a helium-cooled bolometer detector. Figure 2(a) reports the measured transmission spectra of the Tamm cavity-LC metamaterial coupled resonators for different f_{LC} (represented by the colour dots). We observe for each transmission curve two well-separated resonance peaks that form two distinct lower and upper frequency coupled modes. These modes are the result of the coupling between the Tamm cavity and the LC metamaterial. Around the frequency matching between the Tamm cavity mode and the LC metamaterial mode (dark green curve), the two peaks are approximately symmetric and separated by a splitting of 0.20 THz. Figure 2(b) shows the frequencies of the two measured resonance peaks corresponding to the frequency of the upper (red squares) and lower (blue squares) coupled modes as a function of f_{LC}. We clearly observe the two distinct branches forming the anti-crossing pattern, similar to the behavior observed in the strong light–matter coupling regime, demonstrating the strong coupling between the Tamm cavity and the LC metamaterial.

To quantitatively describe the experimentally observed trends, we use a quantum formalism similar to the Rabi Hamiltonian, the Hopfield model [27], which involves bosonic operators only. In a general picture involving two resonators, creation and annihilation operators $\hat{a}^\dagger$, $\hat{a}$ and $\hat{b}^\dagger$, $\hat{b}$ are associated with the photonic modes **A** and **B**. Here, **A** is the Tamm cavity mode, and **B** is the LC metamaterial mode. The Hamiltonian of the coupled resonators can then be expressed as

$$\hat{H} = \hbar\omega_A\left(\hat{a}^\dagger\hat{a} + \frac{1}{2}\right) + \hbar\omega_B\left(\hat{b}^\dagger\hat{b} + \frac{1}{2}\right) + \hbar G\left(\hat{a}^\dagger\hat{b} + \hat{a}\hat{b}^\dagger - \hat{a}\,\hat{b} - \hat{a}^\dagger\hat{b}^\dagger\right), \tag{1}$$

where G is defined here as an energy exchange rate between the two harmonic oscillators. The uncoupled eigenstates are written as $|N_A, N'_B\rangle$ with N, N' the numbers of photons in modes **A** and **B**, respectively. Under the rotating wave approximation and considering for simplicity the subspace with one photon in the system, the eigenstates are two coupled photonic modes $|+_1\rangle$ and $|-_1\rangle$ that are linear combinations of the uncoupled eigenstates $|1_A, 0_B\rangle$ and $|0_A, 1_B\rangle$,

$$\begin{aligned} |+_1\rangle &= \cos\theta|1_A, 0_B\rangle + \sin\theta|0_A, 1_B\rangle, \\ |-_1\rangle &= \sin\theta|1_A, 0_B\rangle - \cos\theta|0_A, 1_B\rangle, \end{aligned} \tag{2}$$

where $\tan(2\theta) = -\frac{2G}{\delta}$. θ varies from 0 to $\frac{\pi}{2}$ with the resonator detuning $\delta = \omega_B - \omega_A$ describing the continuous transition from $|1_A, 0_B\rangle$ to $|0_A, 1_B\rangle$, $\theta = \frac{\pi}{4}$ at zero detuning. The lower (–) and upper (+) resonance angular frequencies read

$$\omega_\pm = \frac{\omega_A + \omega_B}{2} \pm \frac{1}{2}\sqrt{(\omega_A - \omega_B)^2 + 4G^2}. \tag{3}$$

Note that the significant reduction of the resonator coupling constant G when the LC pattern size is reduced (i.e., f_{LC} increases) is accounted for using an empirical linear model $G = G_0(1 - \beta(\omega_B - \omega_A))$; see Appendix B for details and arguments for this description. We find a good quantitative agreement between experiment and theory [Eq. (3)] for $G \approx 0.10$ THz at frequency matching [solid black lines in Fig. 2(b)]. From this analysis, we extract a reduced coupling constant $G/\omega_0 \sim 0.1$ demonstrating the ultrastrong coupling regime between the Tamm cavity and the LC metamaterial.

3. TEMPORAL COUPLED MODE THEORY FOR THE QUALITY FACTOR OF STRONGLY COUPLED RESONATORS

The experimental transmission spectra also provide a measure of the quality factors of the hybrid Tamm cavity-LC metamaterial resonators that we investigate in this section. We report

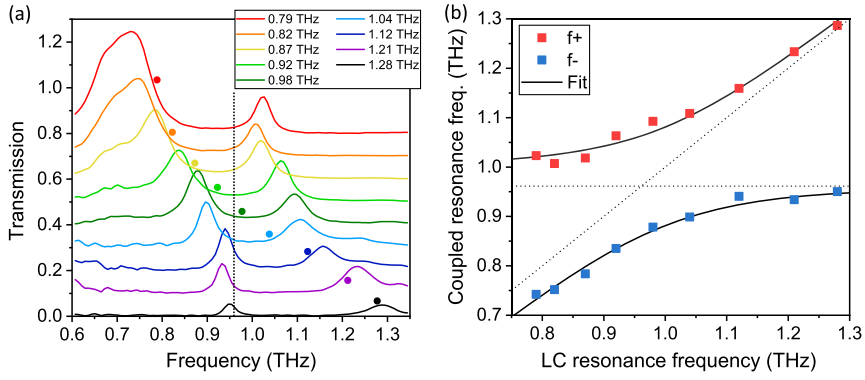

Fig. 2. (a) Transmission spectra of the Tamm cavity-LC metamaterial coupled resonators for decreasing (bottom to top) LC resonance frequencies f_{LC} (indicated by color circles; see legend box). The Tamm cavity resonance is fixed, about 0.96 THz (dotted vertical line). The curves are offset for clarity. (b) Resonance frequencies of the upper (red squares) and lower coupled mode (blue squares) as a function of the uncoupled LC resonance frequency f_{LC} (diagonal dotted line). Horizontal dotted line, uncoupled Tamm cavity resonance frequency.

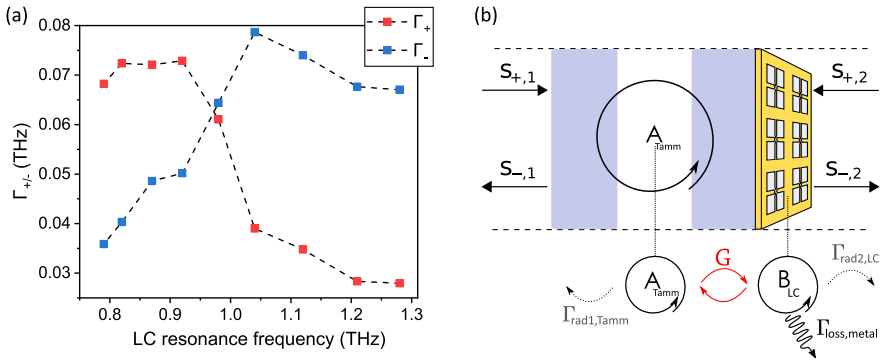

Fig. 3. (a) Resonance peak linewidth of the two coupled modes from Lorentzian fit on data from Fig. 2(a). Dashed lines are guide for the eyes. (b) Schematic picture of the Tamm cavity and LC metamaterial directly on top, including radiative channels s_1 and s_2. Bottom, corresponding interaction scheme between the Tamm mode **A** and the LC metamaterial mode **B** including the relevant coupling rates.

on Fig. 3(a) the evolution of the linewidth of the two resonance peaks $\Gamma_\pm$ as a function of f_{LC}. The two curves exhibit a crossing at zero detuning (corresponding to $f_{\mathrm{LC}} = 0.98$ THz) resulting from the exchange of properties between the Tamm cavity and the LC metamaterial in the coupled modes. At the crossing, we measure $\Gamma_+ = 0.061$ THz and $\Gamma_- = 0.064$ THz yielding the quality factors $Q_+ = 18$ and $Q_- = 14$ for the upper and lower coupled modes. Such values are surprisingly high, considering standard theory of coupled modes [28], which predicts linewidths $\Gamma_\pm = \frac{\Gamma_{\mathrm{Tamm}}+\Gamma_{\mathrm{LC}}}{2} \sim 0.11$ THz resulting in $Q_{\pm,\mathrm{CM}} \approx 9$ (i.e., $Q_{\pm,\mathrm{CM}} \approx 2Q_{\mathrm{LC}}$ since $\Gamma_{\mathrm{Tamm}} \ll \Gamma_{\mathrm{LC}}$).

To understand the physical mechanism underlying these higher than expected Q values of the coupled modes, we use the temporal coupled mode theory [23,29] and analyze the different decay and coupling rates involved in the system. The complete study, which includes the full derivation, the expression of the S-parameters, and the expression of the resonator coupling constant G, is presented in Appendix A. We consider a set of two coupled planar resonators **A** and **B** in a series, exchanging energy radiatively with an input channel s_1 (excited by a wave $s_{+,1}$) and an output channel s_2, respectively, as sketched in Fig. 3(b). The coupled equations of motion are

$$\begin{cases} \frac{\mathrm{d}A}{\mathrm{d}t} = \left(i\omega_A - \frac{\Gamma_A}{2}\right)A + i\sqrt{\frac{C_B}{C_A}}GB + \sqrt{\frac{\Gamma_{\mathrm{rad1},A}}{C_A}}s_{+,1} \\ \frac{\mathrm{d}B}{\mathrm{d}t} = \left(i\omega_B - \frac{\Gamma_B}{2}\right)B + i\sqrt{\frac{C_A}{C_B}}GA \end{cases}, \quad (4)$$

where A and B are the complex field amplitude of mode **A** and **B**, respectively [30], G is the resonator coupling constant, C_A (C_B) defines the relation between the complex field amplitudes A (B) and the mode energy in the resonator $W_A = C_A|A|^2$ ($W_B = C_B|B|^2$), and Γ_A (Γ_B) is the amplitude decay rate of mode **A** (**B**) with $\Gamma_A = \Gamma_{\mathrm{rad1},A} + \Gamma_{\mathrm{loss},A}$ ($\Gamma_B = \Gamma_{\mathrm{rad2},B} + \Gamma_{\mathrm{loss},B}$).

Using this model, we derive the expressions of the reflection and transmission coefficients of the coupled resonator system (see Appendix A) and determine the analytical expression of the resonance linewidth of the upper and lower coupled modes, $\Gamma_\pm$, in the ultrastrong coupling regime. Considering the Tamm cavity as **A** and the LC metamaterial as **B**, $\Gamma_\pm$ reads at zero detuning,

$$\Gamma_\pm = \frac{\Gamma_{\mathrm{rad1,Tamm}} + \Gamma_{\mathrm{rad2,LC}} + \Gamma_{\mathrm{loss,Tamm}} + \Gamma_{\mathrm{loss,LC}}}{2}. \quad (5)$$

In this equation, $\Gamma_{\mathrm{rad1,LC}}$ and $\Gamma_{\mathrm{rad2,Tamm}}$ vanish as the energy emitted by the LC metamaterial in the left direction is absorbed by the Tamm cavity and reciprocally [see Fig. 3(b)]. This coupling mechanism is responsible for the narrow resonance linewidths of the coupled modes observed experimentally in Fig. 3(a) compared to those predicted by the standard theory of coupled modes, which explains the large values of Q_- and Q_+. It also highlights the strong link between the coupling strength and the radiative coupling properties of the LC metamaterial, which is the origin of the large value of G as $\Gamma_{\mathrm{rad1,LC}}$ is the dominant loss term of the uncoupled LC metamaterial, consistently with the expression of G reported in the Appendix C, which scales like $\sqrt{\Gamma_{\mathrm{rad1,LC}}}$.

The resonance linewidth of the coupled modes can be further simplified. Since there is no way to distinguish $\Gamma_{\mathrm{loss,Tamm}}$ from $\Gamma_{\mathrm{loss,LC}}$ as they both result from ohmic losses in the metal layer, we note $\Gamma_{\mathrm{loss,metal}} = \Gamma_{\mathrm{loss,Tamm}} + \Gamma_{\mathrm{loss,LC}}$. Moreover, the DBR mirror is highly reflective, leading to $\Gamma_{\mathrm{rad1,Tamm}} \ll \Gamma_{\mathrm{rad2,LC}}$. The resonance linewidth of the coupled modes reduces then to $\Gamma_\pm \approx \frac{\Gamma_{\mathrm{rad2,LC}}+\Gamma_{\mathrm{loss,metal}}}{2}$. This simplified expression highlights that $\Gamma_\pm$ can be ultimately reduced down to its fundamental limit $\frac{\Gamma_{\mathrm{loss,metal}}}{2}$ by suppressing the radiative losses $\Gamma_{\mathrm{rad2,LC}}$. To this aim, we fabricate Tamm cavity-LC metamaterial coupled resonators and add a supplementary mirror at a distance of 75 μm over the LC metamaterial, which suppresses radiative losses in s_2 at the expense of preventing the use of these hybrid cavities in transmission.

Figure 4 shows the experimental reflection spectra of two Tamm cavity-LC metamaterial coupled resonators based on DBRs made of two and three silicon layers and, respectively, one and two vacuum layers, including the additional gold mirror blocking transmission. We observe two high contrast peaks at resonance frequencies 0.84 and 1.06 THz, with $Q = 25.2 \pm 1.6$ and $Q = 32.6 \pm 1.2$ for the two-silicon-layer-based structure and $Q = 35 \pm 6$ and $Q = 37 \pm 5$ for the three-silicon-layer-based structure. The uncertainty regarding the three layers' cavity quality factor is attributed to the resolution of our setup (6 GHz) combined with limited peak contrast and non-negligible parasitic features in the spectrum.

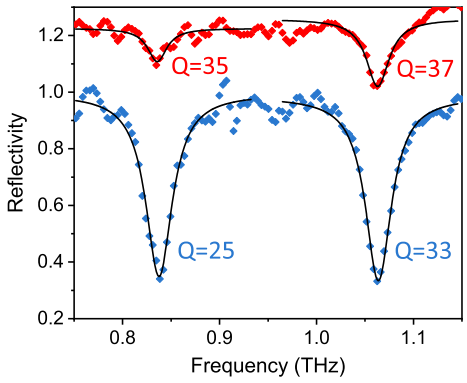

Fig. 4. Reflection spectra of a Tamm cavity resonant at approximately 0.95 THz coupled with an LC metamaterial resonant at 0.92 THz, including an additional mirror blocking the transmission. Blue, two-layer Tamm cavity with $Q = 25.2 \pm 1.6$ and $Q = 32.6 \pm 1.2$ for the lower and upper frequency coupled modes, respectively. Red, three-layer Tamm cavity with $Q = 35 \pm 6$ and $Q = 37 \pm 5$, respectively (0.2 offset for clarity). Solid black lines, Lorentzian fits. Quality factor errors are evaluated from fitting standard deviation.

Increasing the number of silicon layers in the DBR increases its reflectivity and accordingly reduces the value of $\Gamma_{\mathrm{rad1,Tamm}}$ so that the quality factor increases. However, adding more than three layers reduces the peak contrast dramatically because of critical coupling arguments [26].

These results show that our approach improves the quality factor Q by a factor 8 over the uncoupled LC metamaterial. Also, our analysis reveals that the Q enhancement results from the suppression of the dominant decay rate that is the radiation loss rate of the LC metamaterial so that the quality factor is almost ultimately limited by the losses in the metallic layer.

4. MODE VOLUME OF STRONGLY COUPLED RESONATORS

We now examine the mode volume V of the Tamm cavity-LC metamaterial coupled resonators. The unit cell pattern of the LC metamaterial is designed to concentrate the electric field in the central capacitive gap between the metallic tips, and we are interested in how this electric field confinement is modified by the coupling to the Tamm cavity. To this purpose, using the eigenfrequency solver of COMSOL Multiphysics, we compute the electromagnetic field distributions of the lower and upper frequency resonant modes of the coupled resonators. Simulations were run in a single period of the metamaterial bounded by orthogonal perfect electric and perfect magnetic conductor boundary conditions to create the array periodicity, and they are bounded by perfectly matched layers in the propagation direction. The gold layer is modeled using the refractive index of gold interpolated from data from Ref. [31]. Figure 5(a) displays the in-plane electric field amplitude enhancement of the upper coupled mode in the LC metamaterial plane for $f_{\mathrm{LC}} = 1.01$ THz compared to an input plane wave of unity amplitude (see Appendix C for the electric field profile along the optical axis). We observe a large increase of the electric field between the metallic tips and around their edges, reaching a factor up to 20. From the computed electric field distributions, we calculate the effective mode volumes according to the definition used for dissipative resonators [32],

$$V = \frac{\int (\epsilon \boldsymbol{E}^2 - \mu \boldsymbol{H}^2) \mathrm{d}^3 r}{2\epsilon(r_0)\boldsymbol{E}^2(r_0)}, \tag{6}$$

where r_0 is taken at the center of the LC metamaterial pattern in vacuum above the layer surface [$\epsilon(r_0) = \epsilon_0$]. This equation is appropriate in our case as the quality factors of the coupled resonators remain in the range of a few tens. For the following, we consider only the real part $\Re(V)$ of this complex expression. We also compute the mode volume of the uncoupled LC metamaterial on an infinite silicon substrate and obtain $V_{\mathrm{LC}} \approx 1.1 \times 10^{-4}\lambda^3$.

Figure 5(b) reports the calculated volumes of the upper and lower coupled modes V_+ and V_-, respectively, at their resonance angular frequencies ω_+ and ω_- normalized by V_{LC} for increasing values of f_{LC} (i.e., increasing values of detuning $\frac{\delta}{2\pi}$) and a fixed Tamm cavity resonance frequency $f_A = 1$ THz. V_+ and V_- show opposite evolution with f_{LC}: V_+ decreases,

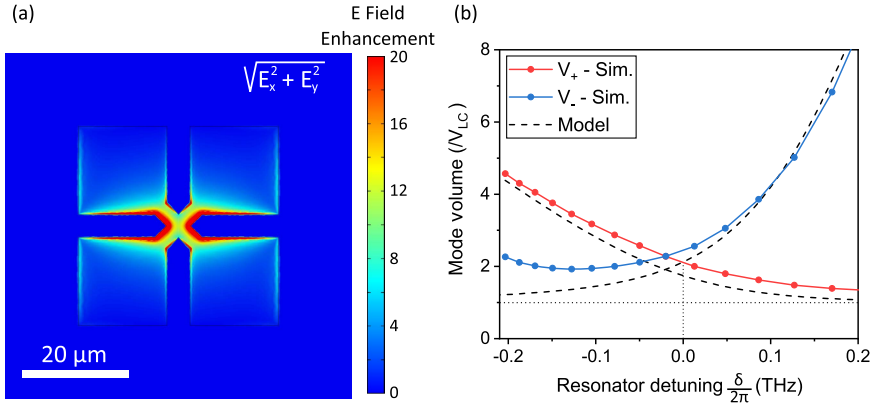

Fig. 5. (a) Distribution of the electric field in the LC metamaterial plane over a single unit cell from FEM simulations for the upper frequency coupled mode at $f_{\mathrm{LC}} = 1.01$ THz. The figure represents the electric field enhancement factor, i.e., the electric field norm for an input wave of amplitude 1. r_0 lies at the center of this picture. (b) Mode volume of upper (red) and lower (blue) frequency coupled modes, normalized by the mode volume of the uncoupled LC metamaterial, as a function of the detuning, from FEM simulation. Dashed line, model from Eqs. (10) and (11). The mode volume values at zero detuning are $3.2 \times 10^{-4}\lambda^3$ for V_+ and $2.0 \times 10^{-4}\lambda^3$ for V_-.

whereas V_- increases when f_{LC} increases. We also observe that the two tendencies cross at a small non-zero detuning $\frac{\delta}{2\pi} = -0.02$ THz. This crossover shows that there is an exchange of mode volume properties between the two resonators similar to the Q properties. This behavior results from the continuous transition of the upper coupled mode from a mode mainly given by the Tamm mode to an LC metamaterial mode for increasing resonator detuning corresponding to the continuous evolution of θ in Eq. (2), and inversely for the lower coupled mode. Thus, V_+ (V_-) converges toward V_{LC} at large positive (negative) detuning, i.e., f_{LC} much higher (lower) than 1 THz. In addition, we note that the mode volume is increased by only a factor ~2.3 compared to V_{LC} at the curve crossing and by factors 2.1 and 2.5 for V_+ and V_-, respectively, at zero detuning. The mode volumes at zero detuning are reduced down to $3.2 \times 10^{-4}\lambda^3$ for V_+ and $2.0 \times 10^{-4}\lambda^3$ for V_-, revealing a high degree of subwavelength confinement of the coupled modes (details are available in Appendix A).

These simulation results raise the question of the origin of the factor 2 in the increase of $V_\pm$ compared to V_{LC}, and the robustness of this value to the designs of the metamaterials and of the Fabry–Perot cavity. To provide some insight, we model the evolution of $V_\pm$ by computing $\langle \pm_1 | \boldsymbol{E}(r)^2 | \pm_1 \rangle$, where $\boldsymbol{E} = \boldsymbol{E}_A(r) + \boldsymbol{E}_B(r)$ is electric field operator, with

$$\begin{aligned} \boldsymbol{E}_A(r) &= i\mathcal{E}_A(a f_A(r) - a^\dagger f_A^*(r)), \\ \boldsymbol{E}_B(r) &= i\mathcal{E}_B(b f_B(r) - b^\dagger f_B^*(r)). \end{aligned} \tag{7}$$

$\mathcal{E}_j = \sqrt{\frac{\hbar\omega_j}{2\epsilon_0 V_j}}$ is the RMS electric field amplitudes associated to vacuum fluctuations in modes $j = A, B$, with V_j defined at the central position r_0. $f_j(r)$ is the electric field amplitude profile of the mode, normalized such that $f_j(r_0) = 1$. We then estimate the mode volume of the coupled mode V_+ using the usual expression involving the electric field only [33],

$$V_+ = \frac{\int \epsilon(r) |\langle +_1 | \boldsymbol{E}(r)^2 | +_1 \rangle| \mathrm{d}^3 r}{\epsilon(r_0) |\langle +_1 | \boldsymbol{E}(r_0)^2 | +_1 \rangle|}. \tag{8}$$

We recognize in the numerator the expression of the electromagnetic energy in the mode, whose value for one photon is directly $\frac{3\hbar\omega_+}{2}$. In the denominator, we use the expressions of the coupled terms from Eq. (2),

$$\begin{aligned} &\langle +_1 | \boldsymbol{E}(r_0)^2 | +_1 \rangle \\ &\quad = \frac{3}{2}\cos^2\theta \mathcal{E}_A^2 + \frac{3}{2}\sin^2\theta \mathcal{E}_B^2 + 2\cos\theta \sin\theta \mathcal{E}_A \mathcal{E}_B, \end{aligned} \tag{9}$$

where $\tan(2\theta) = -\frac{2G}{\delta}$. Then, the coupled mode volume V_+ is expressed as

$$V_+ = \frac{V_B}{\sin^2\theta}\frac{\omega_+}{\omega_B}\frac{1}{1 + \frac{2}{3}\sqrt{\frac{\omega_A}{\omega_B}}\sqrt{\frac{V_B}{V_A}}\cot\theta + \frac{\omega_A}{\omega_B}\frac{V_B}{V_A}\cot^2\theta}, \tag{10}$$

and equivalently for V_-,

$$V_- = \frac{V_B}{\cos^2\theta}\frac{\omega_-}{\omega_B}\frac{1}{1 - \frac{2}{3}\sqrt{\frac{\omega_A}{\omega_B}}\sqrt{\frac{V_B}{V_A}}\tan\theta + \frac{\omega_A}{\omega_B}\frac{V_B}{V_A}\tan^2\theta}. \tag{11}$$

The detailed calculation is reported in Appendix B. Considering resonator **A** stands for the Tamm cavity and resonator **B** for the LC metamaterial, we compare the simulation results in Fig. 5(b) with the calculated $V_\pm$ [Eqs. (10) and (11)] as a function of the resonator detuning and find quantitative agreement for the only free parameter $\alpha = \sqrt{\frac{V_B}{V_A}} = 0.22$ (dashed lines), validating our theoretical description. Note that we take into account the evolution of G with ω_B using $\beta = 0.18$ THz^{-1} determined from fitting the simulated resonance frequencies.

In a simplified picture at small detuning, $\omega_+ \approx \omega_- \approx \omega_B$, and since $V_B \ll V_A$, the coupled mode volumes can be reduced to $V_+ \approx V_B/\sin^2\theta$ and $V_- \approx V_B/\cos^2\theta$. These expressions describe the crossing of the curves at frequency matching ($\delta = 0$ and $\theta = \pi/4$) with $V_\pm = 2V_B$. Thus, our model reproduces the increase of $V_\pm$ by a factor of 2 compared to V_{LC} observed at zero detuning and, importantly, highlights that the mode volumes of the coupled resonator systems are dominated by the metamaterial mode volume at small detuning. The factor 2 can be interpreted as the dilution of the photon electromagnetic energy in the two resonators. Achieving coupled mode volumes of only 2 times, the mode volume of the uncoupled LC metamaterials is then a general result that can be transposed to other coupled systems based on metamaterials and Fabry–Perot cavity. Additionally, the refined model from Eqs. (10) and (11) captures the asymmetry of the $V_\pm$ curves at large detuning, due to the variation of the resonator coupling constant G and the contribution of the mode **A**. Also, our model reproduces the 0.02 THz shift of the mode volume curve crossing due to the symmetric or anti-symmetric contribution of the Tamm mode (mode **A**), which results in $\boldsymbol{E}_+(r_0) \neq \boldsymbol{E}_-(r_0)$ at frequency matching. The deviation for V_- at negative detuning is attributed to the much larger wavelength for f_-.

The present analysis demonstrates that the main strength of LC metamaterials, which is their extremely small mode volume, is preserved despite their coupling to the Fabry–Perot cavity with a very large mode volume, which underlines the main interest of coupling these two distinct types of photonic resonators.

5. HYBRID RESONATORS FOR THz LIGHT–MATTER INTERACTION

The properties of our hybrid THz cavities based on the coupling of LC metamaterials with Tamm cavities are very promising for the development of THz light–matter coupling platforms with a high degree of coherence. Indeed, these hybrid cavities conciliate quality factors of up to a few tens, provided by the Tamm cavity, with sub-wavelength electric field confinement, provided by the LC metamaterial, as summarized in Table 1.

The lower values of the Q that we measured compared to those predicted are most likely due to the significantly lower conductivity of the chromium–gold layer we used for

Table 1. Comparison of V and Q (theoretical and experimental) performances for the LC metamaterial alone, coupled with a 2 silicon layers Tamm cavity, and coupled with a 3 silicon layers Tamm cavity + additional mirror[a]

	LC MM	Tamm(2L)-LC	Tamm(3L)-LC + Mir.
V	$1.1\times10^{-4}\lambda^3$	$3.2\times10^{-4}\lambda^3$	$3.2\times10^{-4}\lambda^3$
Q_{theo}	4.5	32	86
Q_{exp}	/	18	37
$\left(\frac{Q_{\text{theo}}}{V}\right)_{\text{enh.}}$	1	3.1	8.3
$\left(\frac{Q_{\text{exp}}}{V}\right)_{\text{enh.}}$	1	1.9	3.6

[a] Q/V values are normalized to the values of the uncoupled LC metamaterial to show the enhancement due to the coupling and we considered the upper frequency coupled mode; the Tamm(2L)-LC data are from Fig. 2(a) and the Tamm(3L)-LC + Mir. data are from Fig. 4.

fabrication compared to the pure gold layer we consider in the simulation, which opens up opportunities for future improvements.

6. CONCLUSION

In conclusion, we have experimentally and theoretically investigated original hybrid THz cavities based on the ultrastrong coupling between a THz Tamm cavity and an LC circuit metamaterial. We have demonstrated Q of up to 37 associated with V as low as $3.2\times10^{-4}\lambda^3$. Our work shows that the principal qualities of resonators, which are a high Q for Tamm cavity and a low V for LC circuit metamaterials, act beneficially in the presence of the coupling. Compared to the uncoupled LC metamaterial, Q is enhanced by a factor of 8 due to the coupling with a Tamm cavity, while V is increased by only a factor of ∼2 as a result of the energy dilution within the two resonators. Thus, investigating light–matter interaction using these hybrid THz cavities should provide a high degree of coherence due to the enhancement of the cooperativity C of at least 3.8, opening interesting perspectives for the development of single photon THz emitters and detectors [34] and quantum technology applications. Also this hybrid system compares favorably to uncoupled LC metamaterials for the study of light–matter interaction in the ultrastrong coupling regime with quantum material having low non-radiative decay rates γ, as the reduction of g given by $1/\sqrt{V}$ remains small compared to the reduction of the resonator linewidth κ. Furthermore, our analysis revealed the suppression of the radiative losses of the LC metamaterials when embedded in the Tamm cavity so that the quality factor is ultimately limited by the ohmic losses of the metallic layer. This property opens vast possibilities in the development of new LC metamaterial patterns previously disregarded due to large radiative losses and renews the interest of investigating low-loss metamaterials based on superconducting materials [35,36] to reach very high Q values. Additionally, our theoretical description of the variations of the mode volume due to the coupling evidences the generality of this concept: possible metamaterials are not limited to the hole array LC circuit we presented but could also include direct split ring resonators similar to Ref. [20] as well as micro-antennas.

APPENDIX A: TEMPORAL COUPLED MODE THEORY FOR S-PARAMETERS OF COUPLED RESONATOR SYSTEMS AND EVALUATION OF THE COUPLING CONSTANT G

We present here the study of a system of two coupled resonators using the temporal coupled mode theory (temporal CMT), which is used to describe extensively the properties of single resonators in Refs. [23,29]. We will detail here the equations associated with this model to provide the expressions of reflection and transmission coefficients. In particular, we will show which parameters influence the value of the resonator coupling constant G.

1. Equation of Motion of the Two Coupled Resonators

We consider a set of two coupled resonators **A** and **B** to which two resonant modes at uncoupled angular frequencies ω_A and ω_B are associated. The field amplitudes in the respective modes are noted as A and B. These resonators are associated here "inline," i.e., resonator **A** is coupled to an input propagation channel s_1 and resonator **B** to an output propagation channel s_2, and transmission is only possible by passing through both resonators **A** and **B** (see Fig. 6). This corresponds to the scenario of the Tamm cavity coupled to a resonant LC circuit metamaterial deposited on its top mirror. We note that κ_i^* is the incoming wave $s_{+,\mu}$ to resonant mode i coupling constant, t_i is the resonant mode i to outgoing wave $s_{-,\mu}$ coupling constant, and $\gamma_i=\frac{1}{\tau_{\text{loss},i}}$ is the amplitude non-radiative decay rate. We use notation t_i and r_i as these coefficients identify to the amplitude transmission and reflection coefficients in typical optical resonators such as Fabry–Perot cavities.

From an energy point of view, there is a quadratic relation between the amplitude X_i (i.e., A or B) and the energy stored in the resonator W_i, $W_i=C_i|X_i|^2$, as presented in Ref. [37]. The parameter C_i describes in the general case the energy capacity of the system for a given field amplitude. This additional complexity compared to a simpler definition $W_i=|X_i|^2$ offers in fact an additional degree of freedom enabling the comparison between different resonators having different C_i. There is indeed a direct relation between the mode volume and the coefficient C_i: using our notation, the mode volume V is actually defined as $V_i=\frac{W_i}{\epsilon|E_i|^2}$. We deduce that C_i defined here is proportional to the mode volume V_i.

A reciprocity relation between κ_i^* and t_i can be deduced from time reversal symmetry arguments as presented in Ref. [29],

$$\kappa_i^*=\frac{t_i}{C_i}. \tag{A1}$$

We can now write the equation of motion for amplitudes A and B,

$$\begin{cases}\frac{dA}{dt}=\left(i\omega_A-\frac{1}{\tau_A}\right)A+ig_A^*B+\frac{t_A}{C_A}s_{+,1}, & \frac{1}{\tau_A}=\frac{|t_A|^2}{2C_A}+\frac{1}{\tau_{\text{loss},A}},\\ \frac{dB}{dt}=\left(i\omega_B-\frac{1}{\tau_B}\right)B+ig_B^*A, & \frac{1}{\tau_B}=\frac{|t_B|^2}{2C_B}+\frac{1}{\tau_{\text{loss},B}},\end{cases} \tag{A2}$$

as well as the expressions of the waves radiated from the resonator $s_{-,1}$ and $s_{-,2}$,

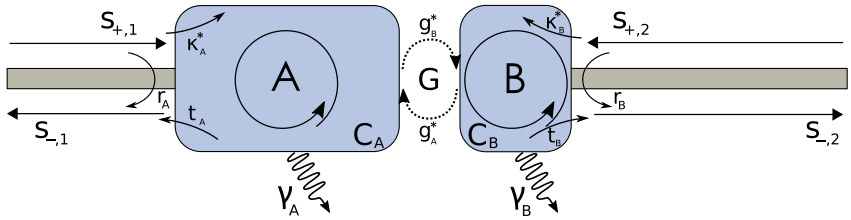

Fig. 6. Schematic coupling scheme between resonators **A** and **B**, as well as input and output propagation channels s_1 and s_2.

$$s_{-,1} = r_A s_{+,1} + t_A A \quad \text{and} \quad s_{-,2} = r_B s_{+,2} + t_B B. \tag{A3}$$

2. Homogeneous Harmonic Solutions

The resonance frequencies $\omega_\pm$ of this coupled resonator system are given by the associated homogeneous system in the frequency domain,

$$\begin{cases} 0 = \left(i(\omega_A - \omega) - \frac{1}{\tau_A}\right)A + ig_A^* B \\ 0 = \left(i(\omega_B - \omega) - \frac{1}{\tau_B}\right)B + ig_B^* A \end{cases}. \tag{A4}$$

The characteristic equation reads

$$0 = g_A^* g_B^* + \left(i(\omega_A - \omega) - \frac{1}{\tau_A}\right)\left(i(\omega_B - \omega) - \frac{1}{\tau_B}\right) \tag{A5}$$

or

$$0 = g_A^* g_B^* - \omega^2 + \omega\left((\omega_A + \omega_B) + i\left(\frac{1}{\tau_A} + \frac{1}{\tau_B}\right)\right) - i\left(\frac{\omega_A}{\tau_B} + \frac{\omega_B}{\tau_A}\right) + \frac{1}{\tau_A \tau_B} - \omega_A \omega_B. \tag{A6}$$

If the losses are negligible, this equation is reduced to

$$0 = g_A^* g_B^* - \omega^2 + \omega(\omega_A + \omega_B) - \omega_A \omega_B, \tag{A7}$$

from which the solutions are straightforward,

$$\omega_\pm = \frac{\omega_A + \omega_B}{2} \pm \sqrt{\frac{(\omega_A - \omega_B)^2}{4} + g_A^* g_B^*}. \tag{A8}$$

We should stress here that this result shows that the temporal CMT we present here describes the strong resonator coupling regime for $\frac{g_i^*}{\omega_i} < 0.1$ as the solution we find here matches the form resulting from the rotating wave approximation of the Hopfield model.

3. Temporal Solutions and Exchange Factors g_i^*

As g_A^* and g_B^* describe reciprocal phenomena of coherent transfer from **B** to **A** and from **A** to **B**, respectively, there is obviously a relation between these two exchange factors. We can derive this relation using energy conservation arguments in a particular scenario. We consider here the case of two lossless coupled resonators, only exchanging energy between each other with $\begin{pmatrix} A \\ B \end{pmatrix} = \begin{pmatrix} 1 \\ 0 \end{pmatrix}$ at $t = 0$, and we look for the time domain solution of the following form:

$$\begin{pmatrix} A \\ B \end{pmatrix} = \begin{pmatrix} \alpha(t) \\ \beta(t) \end{pmatrix} e^{i\omega t}.$$

The general system of equation for $\alpha(t)$, $\beta(t)$ is deduced from Eq. (A2),

$$\begin{cases} \frac{d\alpha}{dt}(t) = i(\omega_A - \omega)\alpha(t) + ig_A^* \beta(t) \\ \frac{d\beta}{dt}(t) = i(\omega_B - \omega)\beta(t) + ig_B^* \alpha(t) \end{cases}, \tag{A9}$$

at resonance and frequency matching of the resonators, $\omega = \omega_A = \omega_B$. The solution is then directly

$$\begin{pmatrix} \alpha(t) \\ \beta(t) \end{pmatrix} = \begin{pmatrix} \cos(Gt) \\ i\frac{G}{g_A^*}\sin(Gt) \end{pmatrix}, \quad \text{with} \quad G^2 = g_A^* g_B^*. \tag{A10}$$

Two coupled resonators isolated from outside coupling, thus, have their amplitude modulated with a $\frac{\pi}{2}$ dephasing, with a frequency given by the resonator coupling constant G, in a similar manner to Rabi oscillations. Using the argument of energy conservation, we can then deduce a relation between g_A^* and g_B^*. The temporal evolution of the total energy in the system $W(t)$ is written as

$$\begin{aligned} W(t) &= C_A|A(t)|^2 + C_B|B(t)|^2 \\ &= C_A \cos^2(Gt) + C_B\left(\frac{G}{g_A^*}\right)^2 \sin^2(Gt). \end{aligned} \tag{A11}$$

Energy conservation is then only fulfilled if

$$C_A g_A^* = C_B g_B^*. \tag{A12}$$

We can then define in a symmetrical form

$$g_A^* = \frac{g^*}{C_A} \quad \text{and} \quad g_B^* = \frac{g^*}{C_B}, \tag{A13}$$

with g^* being the dimensionless amplitude exchange coefficient between resonators **A** and **B**, defined in a similar manner to the coupling coefficients t_i to the propagation channels in $\frac{t_i}{C_i}$ [see Eq. (12)]. Under this formulation, the expression of the resonator coupling constant becomes

$$G = \frac{g^*}{\sqrt{C_A C_B}}. \tag{A14}$$

We show this way the explicit dependence of G, which is the main observable in resonator strong coupling experiments versus the resonators energy capacities C_i, and identify g^* as the true irreducible parameter characteristic of the coupling. It is especially useful, for instance, in Fabry–Perot cavities of length L and group velocity v_g, for which we know $C_{\mathrm{FP}} = \frac{2L}{v_g}$ is given by the round trip time between the two mirrors inside the cavity [38]. We expect then G to scale like $L^{-\frac{1}{2}}$ in Fabry–Perot-type cavities. This formula matches the findings of Meng *et al.* in Ref. [22], where the authors coupled complementary split ring resonators (CSRRs) to a Tamm cavity and studied several thicknesses for the Tamm cavity layers using CST simulations, showing a $\frac{1}{\sqrt{V_A}}$ dependence of the resonator coupling constant G.

4. General Case: Expression of S-Parameters

We will come back to general case of a pair of coupled resonators excited by an input wave $s_{+,1}$. The equations of motion in the frequency domains read

$$\begin{cases} \frac{t_A}{C_A} s_{+,1} = \left(i(\omega_A - \omega) - \frac{1}{\tau_A}\right) A + i\frac{g^*}{C_A} B \\ 0 = \left(i(\omega_B - \omega) - \frac{1}{\tau_B}\right) B + i\frac{g^*}{C_B} A \end{cases}, \tag{A15}$$

from which we derive the expressions of the amplitudes $A(\omega)$ and $B(\omega)$ inside the resonators,

$$A(\omega) = \frac{\left(i(\omega - \omega_B) + \frac{1}{\tau_B}\right) + \frac{t_A}{C_A} s_{+,1}}{\left(i(\omega - \omega_A) + \frac{1}{\tau_A}\right)\left(i(\omega - \omega_B) + \frac{1}{\tau_B}\right) + G^2},$$

$$B(\omega) = \frac{i\frac{g^*}{C_B}\frac{t_A}{C_A} s_{+,1}}{\left(i(\omega - \omega_A) + \frac{1}{\tau_A}\right)\left(i(\omega - \omega_B) + \frac{1}{\tau_B}\right) + G^2}. \tag{A16}$$

We can deduce the expression of the global reflection and transmission coefficients r and t from their expressions within the model,

$$r = \frac{s_{-,1}}{s_{+,1}} = r_A + \frac{A}{s_{+,1}} t_A \quad \text{and} \quad t = \frac{s_{-,2}}{s_{+,1}} = \frac{B}{s_{+,1}} t_B \tag{A17}$$

so that we have (using $t_A = -r_A t_A^*$ for r [29])

$$r(\omega) = r_A \frac{\left(i(\omega - \omega_B) + \frac{1}{\tau_B}\right)\left(i(\omega - \omega_A) + \frac{1}{\tau_A} - \frac{T_A}{C_A}\right) + G^2}{\left(i(\omega - \omega_A) + \frac{1}{\tau_A}\right)\left(i(\omega - \omega_B) + \frac{1}{\tau_B}\right) + G^2}, \tag{A18}$$

in which r_A most of the time is simplified to −1, and we noted $T_A = |t_A|^2$ as the power transmission coefficient of the left barrier of resonator **A**. Also,

$$t(\omega) = \frac{i\frac{g^* t_A t_B}{C_A C_B}}{\left(i(\omega - \omega_A) + \frac{1}{\tau_A}\right)\left(i(\omega - \omega_B) + \frac{1}{\tau_B}\right) + G^2}. \tag{A19}$$

5. Power Reflection and Transmission Coefficients

The full expressions of power reflection and transmission coefficients read

$$R = \frac{\left(G^2 - (\omega - \omega_A)(\omega - \omega_B) + \frac{1}{\tau_B}\left(\frac{1}{\tau_A} - \frac{T_A}{C_A}\right)\right)^2 + \left((\omega - \omega_B)\left(\frac{1}{\tau_A} - \frac{T_A}{C_A}\right) + \frac{1}{\tau_B}(\omega - \omega_A)\right)^2}{\left(G^2 - (\omega - \omega_A)(\omega - \omega_B) + \frac{1}{\tau_A}\frac{1}{\tau_B}\right)^2 + \left(\frac{1}{\tau_A}(\omega - \omega_B) + \frac{1}{\tau_B}(\omega - \omega_A)\right)^2} \tag{A20}$$

and

$$T = \frac{G^2 \frac{T_A}{C_A}\frac{T_B}{C_B}}{\left(G^2 - (\omega - \omega_A)(\omega - \omega_B) + \frac{1}{\tau_A}\frac{1}{\tau_B}\right)^2 + \left(\frac{1}{\tau_A}(\omega - \omega_B) + \frac{1}{\tau_B}(\omega - \omega_A)\right)^2}. \tag{A21}$$

It is convenient to use an alternative form using the power coupling rates Γ_i instead of transmission coefficients and energy capacities. Γ_i are defined as

$$\Gamma_{\text{rad1/2},i} = \frac{2}{\tau_{\text{rad},i}} = \frac{T_i}{C_i}, \qquad \Gamma_{\text{loss},i} = \frac{2}{\tau_{\text{loss},i}}, \quad \text{with} \quad \frac{1}{\tau_i} = \frac{1}{\tau_{\text{rad},i}} + \frac{1}{\tau_{\text{loss},i}} = \frac{\Gamma_i}{2}. \tag{A22}$$

In the end, we have

$$R = \frac{\left(G^2 - (\omega - \omega_A)(\omega - \omega_B) + \frac{\Gamma_B}{2}\left(\frac{\Gamma_A}{2} - \Gamma_{\text{rad1},A}\right)\right)^2 + \left((\omega - \omega_B)\left(\frac{\Gamma_A}{2} - \Gamma_{\text{rad1},A}\right) + \frac{\Gamma_B}{2}(\omega - \omega_A)\right)^2}{\left(G^2 - (\omega - \omega_A)(\omega - \omega_B) + \frac{\Gamma_A \Gamma_B}{4}\right)^2 + \left(\frac{\Gamma_A}{2}(\omega - \omega_B) + \frac{\Gamma_B}{2}(\omega - \omega_A)\right)^2} \tag{A23}$$

and

$$T = \frac{G^2 \Gamma_{\text{rad1},A} \Gamma_{\text{rad2},B}}{\left(G^2 - (\omega - \omega_A)(\omega - \omega_B) + \frac{\Gamma_A \Gamma_B}{4}\right)^2 + \left(\frac{\Gamma_A}{2}(\omega - \omega_B) + \frac{\Gamma_B}{2}(\omega - \omega_A)\right)^2}. \tag{A24}$$

R and T are plotted in Fig. 7 for parameters compatible with the coupling of a Tamm cavity and an LC metamaterial. They behave as local Lorentzian peaks around the zeros of $G^2 - (\omega - \omega_A)(\omega - \omega_B) + \frac{\Gamma_A \Gamma_B}{4}$, i.e., the coupled mode resonance frequencies, provided the resonator is in the strong coupling regime.

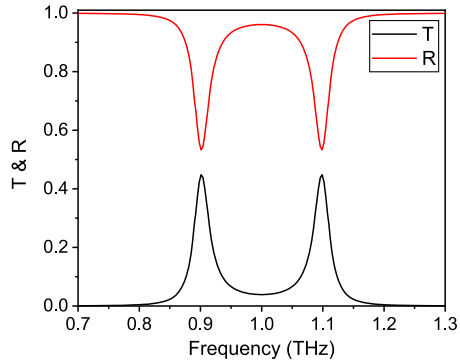

Fig. 7. Theoretical reflection and transmission spectra of the coupled resonator system from Eqs. (A23) and (A24). We used $f_A = f_B = 1$ THz, $G = 0.1$ THz, $\Gamma_A = 0.01$ THz, $\Gamma_B = 0.05$ THz, $\Gamma_{\mathrm{rad1},A} = 0.008$ THz, and $\Gamma_{\mathrm{rad2},B} = 0.045$ THz.

6. Critical Coupling in Coupled Resonator Systems

We are interested here in the values of the power reflection and transmission coefficients for a system of two coupled resonators with the same uncoupled resonance frequency ω_0, at resonance, i.e., for $\omega = \omega_\pm = \omega_0 \pm G$. R and T are then reduced to

$$R = \frac{\Gamma_B^2\left(\frac{\Gamma_{\mathrm{loss},A}-\Gamma_{\mathrm{rad1},A}}{2}\right)^2 + G^2(\Gamma_{\mathrm{loss},A}+\Gamma_{\mathrm{loss},B}+\Gamma_{\mathrm{rad2},B}-\Gamma_{\mathrm{rad1},A})^2}{\left(\frac{\Gamma_A\Gamma_B}{2}\right)^2 + G^2(\Gamma_A+\Gamma_B)^2},$$

$$T = \frac{4G^2\Gamma_{\mathrm{rad1},A}\Gamma_{\mathrm{rad2},B}}{\left(\frac{\Gamma_A\Gamma_B}{2}\right)^2 + G^2(\Gamma_A+\Gamma_B)^2}. \quad \textbf{(A25)}$$

Depending on the coupling regime, we can then identify two different critical coupling regimes.

- In the weak-coupling regime $G < \Gamma_A, \Gamma_B$, only the left part of the above expressions is relevant, T is low, and R reduces to its expression for the resonator **A** only, hence the suppression of R at resonance for

$$\Gamma_{\mathrm{loss},A} = \Gamma_{\mathrm{rad1},A}, \quad \textbf{(A26)}$$

which is basically the critical coupling criterion for resonator **A**.

- In the strong coupling regime $G > \Gamma_A, \Gamma_B$, the right part of the expression is dominant, the contribution of G vanishes, and we find the suppression of R for

$$\Gamma_{\mathrm{rad1},A} = \Gamma_{\mathrm{loss},A} + \Gamma_{\mathrm{loss},B} + \Gamma_{\mathrm{rad2},B}, \quad \textbf{(A27)}$$

as well as a unitary T possible only without losses and for $\Gamma_{\mathrm{rad1},A} = \Gamma_{\mathrm{rad2},B}$. In the strong coupling regime, the system of coupled resonators behaves as a single resonator with $\Gamma_{\mathrm{rad1}} = \frac{\Gamma_{\mathrm{rad1},A}}{2}$, $\Gamma_{\mathrm{rad2}} = \frac{\Gamma_{\mathrm{rad2},B}}{2}$, and $\Gamma_{\mathrm{loss}} = \frac{\Gamma_{\mathrm{loss},A}+\Gamma_{\mathrm{loss},B}}{2}$.

7. Estimation of g^* on Model System

We presented in the previous section the spectral properties of coupled resonator systems and highlighted the importance of the energy capacity C_i. However, one question remains: what is the value of the amplitude exchange coefficient g^*? It is expected to depend on the coupling mechanism and is, hence, specific to each coupling scenario.

The radiative exchanges involved for a single LC metamaterial on an infinite substrate are illustrated in Fig. 8(a). By comparison, the coupling and radiative exchanges involved for a Tamm cavity coupled to a resonant LC metamaterial deposited on its top mirror, illustrated in Fig. 8(b), suggest that the coefficient g^* is linked to the amplitude radiative coupling coefficient in the substrate $t_{1,\mathrm{LC}}$, as the exchange mechanism seems to be the radiative emission of the metamaterial inside the Tamm cavity.

Using FEM simulation, we can study the evolution of the resonator coupling constant G versus the metamaterial period p but also the evolution of the radiative coupling rate $\Gamma_{\mathrm{rad1,LC}}$ from resonance peak linewidth of a single LC metamaterial on an infinite substrate. We choose as model LC resonant metamaterial the CSRR developed in Ref. [39] because its relatively high quality factor (typically $Q > 10$ without metal losses) enables clear results not perturbed by peak asymmetry. We can then evaluate numerically

$$\Gamma_{\mathrm{rad1,LC}} = \frac{|t_{1,\mathrm{LC}}|^2}{C_{\mathrm{LC}}} \quad \text{and} \quad G = \frac{g^*}{\sqrt{C_{\mathrm{Tamm}}C_{\mathrm{LC}}}}. \quad \textbf{(A28)}$$

The values of the resonator coupling constant G and the radiative coupling rate of the uncoupled CSRR to the substrate $\Gamma_{\mathrm{rad1,LC}}$ are represented as a function of the metamaterial period p in Fig. 9.

As suggested by the log plot Fig. 9(b), there is a power law relation between the coupling rates and the metamaterial

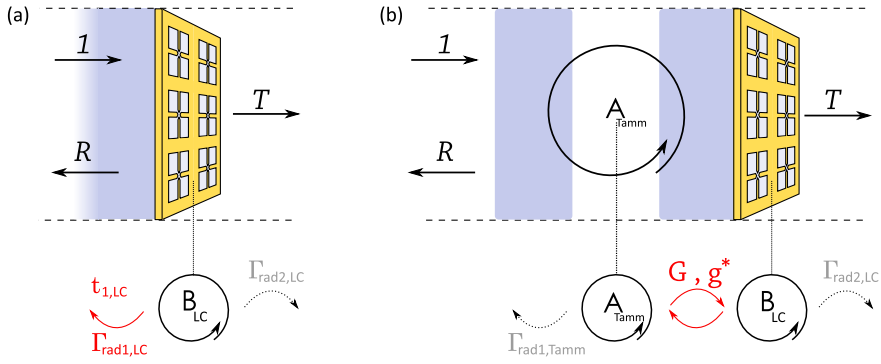

Fig. 8. Schematic pictures of the resonators under study, including input illumination "1" for (a) the LC circuit metamaterial on an infinite silicon substrate and (b) the Tamm cavity coupled to the LC circuit metamaterial directly on top. Bottom, corresponding interaction scheme between the Tamm mode **A** and the LC circuit metamaterial mode **B** including the relevant coupling rates.

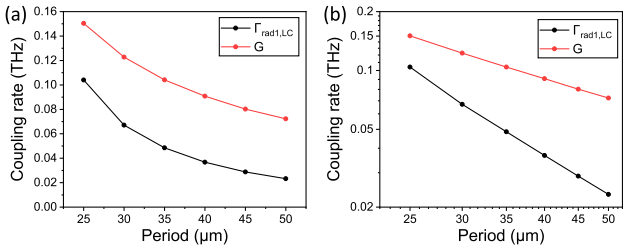

Fig. 9. Evolution of the radiative coupling rate to the substrate $\Gamma_{rad1,LC}$ and of the resonator coupling constant G from FEM simulations. (a) Linear scale; (b) log scale.

period p. Linear fits yield power 2.15 for $\Gamma_{rad1,LC}$ and power 1.05 for G. Assuming that the deviation from integer values in simulations is expected to be due to variation of proximity effects as the LC metamaterial period changes, we can express approximately

$$\Gamma_{rad1,LC} \propto n_{LC} \quad \text{and} \quad G \propto (n_{LC})^{\frac{1}{2}}, \tag{A29}$$

with n_{LC} being the LC resonators density. These results are expected from a super-radiance-based interpretation of the radiative coupling of LC metamaterials. As the electric field radiated coherently by the metamaterial scales like the resonator density n_{LC}, the amplitude radiative coupling coefficient $t_{1,LC}$ scales like n_{LC}. On the other hand, C_{LC} scales like n_{LC}, yielding the power law results we reproduced by simulations.

In more detail, we can find an empirical relation between g^* and $t_{1,LC}$. C_{Tamm} can be evaluated analytically [26], which is unfortunately not easily done for C_{LC}. However, from Eq. (A28), this problem is lifted through the evaluation of the following ratio:

$$\frac{G^2 C_{Tamm}}{\Gamma_{rad1,LC}} = \frac{(g^*)^2}{|t_{1,LC}|^2}, \tag{A30}$$

with $C_{Tamm} = 0.71\ \text{THz}^{-1}$. As expected from the power law dependence, we found this ratio to be constant, equal to about 3.2, which is close to the value of the refractive index of the silicon substrate $n_{Sub} = 3.42$. As a demonstration, we plot in Fig. 10 $\Gamma_{rad1,LC}$ alongside $G^2 C_{Tamm} n_{Sub}$, which shows an excellent agreement, up to a small correction most likely due to an effective refractive index. As a conclusion, we have

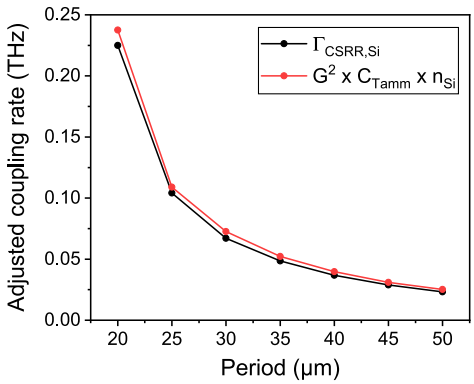

Fig. 10. Comparison of the radiative coupling rate to the substrate of a CSRR metamaterial $\Gamma_{rad1,LC}$ versus the product $G^2 C_{Tamm} n_{Sub}$ from FEM simulations, showing excellent empirical agreement.

shown the direct relation between the large radiative coupling of LC metamaterials and the strong resonator coupling constant G as there is a straightforward linear dependence between g^* and $t_{1,LC}$,

$$g^* = \sqrt{n_{Sub}}|t_{1,LC}|. \tag{A31}$$

APPENDIX B: EVOLUTION OF $\Gamma_{rad1,LC}$ VERSUS f_{LC} AND APPROXIMATE MODEL FOR THE EVOLUTION OF G

In Fig. 2(b) of the main text, we observe in the anti-crossing of the upper and lower resonance frequencies an asymmetry between negative and positive detunings δ. We attribute this feature to the decrease of the resonator coupling constant G when the uncoupled LC resonance frequency f_{LC} increases, which results from the reduction of the LC circuit pattern size. We estimate in this section the expected variations of G with f_{LC} using $G \propto \sqrt{\Gamma_{rad1,LC}}$ as demonstrated in the previous section.

We can estimate $\Gamma_{rad1,LC}$ using FEM simulations from COMSOL Multiphysics. In order to measure $\Gamma_{rad1,LC}$ only, we simulate the LC metamaterial on an infinite silicon substrate, excited with an input wave from the silicon side, and include an additional mirror on top of the structure to prevent transmission of the structure so that $\Gamma_{rad2,LC} = 0$. Also, the metal layer is modeled as a perfect electric conductor to ensure $\Gamma_{loss,LC} = 0$. The resulting system presents no transmission and no absorption so that the power coefficients are trivial with $R = 1$ and $T = A = 0$, preventing the simple measurement of $\Gamma_{rad1,LC}$. We, thus, include artificially a small amount of losses by modeling the additional mirror as a gold layer with finite conductivity so that we can directly measure the resonance linewidth $\Gamma_{rad1,LC}$ on the non-zero (of the order of 0.1%) absorbance peak.

Figure 11(a) represents the resulting spectra for different LC pattern sizes corresponding to different resonance frequencies f_{LC} (legend box). We observe an important reduction of the peak width when f_{LC} increases.

We observe a clear linear evolution of $\Gamma_{rad1,LC}$ with f_{LC} in Fig. 11(b), which we fit with a linear function in the form $\Gamma_{rad1,LC} = \Gamma_0(1 - \beta'(f_{LC} - f_0))$, $f_0 = 1$ THz, and we find $\Gamma_0 = 0.1389$ THz and $\beta' = 2.796\ \text{THz}^{-1}$. Finally, since $G \propto \sqrt{\Gamma_{rad1,LC}}$, we have $\frac{G}{G_0} = \sqrt{\frac{\Gamma_{rad1,LC}}{\Gamma_0}}$, and we can propose a linear expansion for G around $\frac{\omega_A}{2\pi} = 1$ THz in the form $G = G_0(1 - \beta(\omega_B - \omega_A))$ with $\beta = \frac{1}{2}\frac{\beta'}{2\pi} = 0.22\ \text{THz}^{-1}$.

In our measurement presented in Fig. 2(b) of the main manuscript, the variability we observe prevents the precise determination of β, and we find $\beta \approx 0.13 \pm 0.11\ \text{THz}^{-1}$ from curve fitting using Eq. (3) of the main manuscript and the linear model for G, which remains a consistent value. This model explains the reason for the asymmetry we observe in Fig. 2(b) of the main manuscript.

APPENDIX C: ELECTRIC FIELD PROFILE ALONG THE OPTICAL AXIS

We present in Fig. 12 the electric field profile inside the cavity for the higher and lower frequency coupled modes, with and

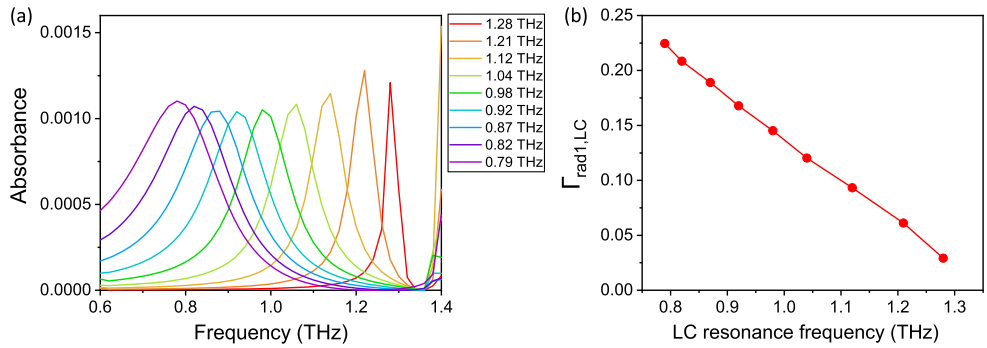

Fig. 11. (a) Resonance peak of an uncoupled LC metamaterial on an infinite silicon substrate with transmission blocked for increasing f_{LC} from FEM simulations. (b) Radiative coupling rate to the substrate of the LC metamaterial $\Gamma_{rad1,LC}$ as a function of f_{LC}, deduced from (a).

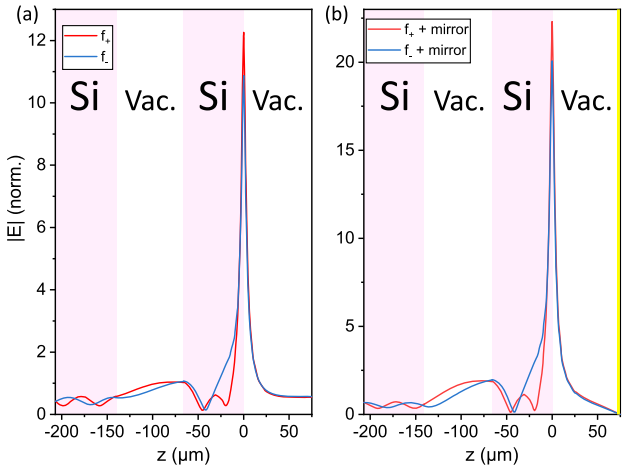

Fig. 12. Electric field enhancement along the optical axis for the higher (red) and lower (blue) resonant coupled modes, without (left) and with (right) the additional mirror. The cut axes intersect the metamaterial plane at the center of the metamaterial unit cell. The cavity is illuminated from the left with a plane wave of unity amplitude, the LC metamaterial is located at $z = 0$, and the additional mirror is located at $z = +75$ μm.

without an additional mirror, from FEM simulations. We primarily notice the large electric field concentration in the $z = 0$ plane corresponding to the LC metamaterial plane. Also, the different scales for the electric field are mainly explained by the quality factor increase in the presence of an additional mirror. Finally, the additional zero of the electric field around $z = -20$ μm for f_+ is revealing of the symmetric (f_-) or anti-symmetric (f_+) coupling between the Tamm and LC metamaterial modes.

APPENDIX D: ADDITIONAL FIGURES FOR THE EVOLUTION OF THE MODE VOLUME FROM FEM SIMULATIONS

We simulate the resonant modes of the coupled Tamm-LC metamaterial (GSRR) structure and of the uncoupled LC metamaterial on an infinite silicon substrate using the eigenfrequency solver of COMSOL Multiphysics. Simulations were run in a single period of the metamaterial bounded by orthogonal perfect electric and perfect magnetic conductor boundary conditions to create the array periodicity, bounded by perfectly matched layers in the propagation direction. Since the quality factors of the coupled resonators are rather low, in the 10 to 50 range, we use for the mode volume the improved formula from Ref. [32] as follows:

$$V = \frac{\int (\epsilon \boldsymbol{E}^2 - \mu \boldsymbol{H}^2) \mathrm{d}^3 r}{2\epsilon(r_0)\boldsymbol{E}^2(r_0)}, \tag{D1}$$

where r_0 is taken at the center of the metamaterial pattern in vacuum above the surface [$\epsilon(r_0) = \epsilon_0$]. From this complex expression, we kept only the real part $\Re(V)$. The mode volumes of the uncoupled metamaterial (V_{GSRR}) and of the upper (V_+) and lower (V_-) frequency coupled modes as a function of the detuning ($\frac{\delta}{2\pi}$) are represented in Fig. 13(a). Figure 13(b) represents the mode volumes V_{GSRR}, V_+, and V_- normalized by the typical volume λ^3, where λ is taken at the actual resonance frequency, i.e., $\lambda(\omega_-)$ is larger than $\lambda(\omega_+)$ for a given detuning δ.

APPENDIX E: DERIVATION OF THE MODE VOLUME OF STRONGLY COUPLED RESONATORS

In this section, we derive an expression for the mode volume of the coupled modes $V_\pm$ of two strongly coupled resonators **A** and **B** as a function of the mode volume of the uncoupled modes V_A and V_B.

We consider two modes **A** and **B** forming a normal basis on which we can write the electric field in the coupled resonators as

$$E(r,t) = \sum_{\text{mode } j} \alpha_j(t) f_j(r). \tag{E1}$$

$\alpha_j(t)$ is the complex amplitude of the mode, accounting for the temporal evolution. $f_j(r)$ is a solution of the Helmholtz equation, i.e., is the electric field amplitude profile of the mode, normalized at a reference point r_0 such that $f_j(r_0) = 1$, with r_0 being usually the point at which the electric field is maximum. In order to ensure coherence between definitions of the mode volume V and f, V should be defined as well at the position r_0, so we write

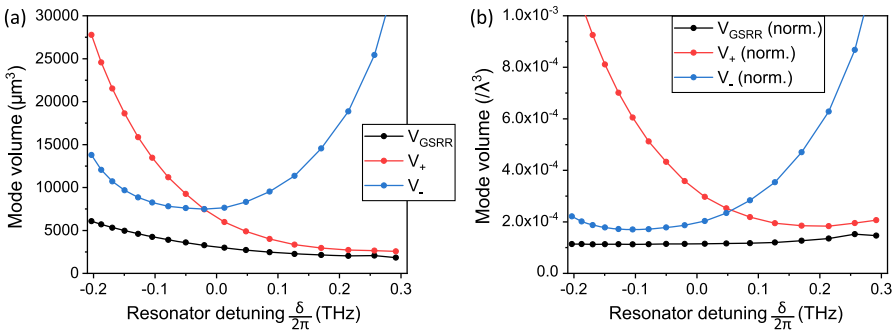

Fig. 13. (a) Mode volume of the uncoupled metamaterial (black) and of the upper (red) and lower (blue) frequency coupled modes, computed from COMSOL simulation. (b) Same, normalized by the value of λ^3 at the resonance frequency.

$$V = \frac{\int \epsilon(r)|E(r)|^2 \mathrm{d}^3 r}{\epsilon(r_0)|E(r_0)|^2} = \int \frac{\epsilon(r)}{\epsilon_0}|f(r)|^2 \mathrm{d}^3 r. \tag{E2}$$

We recall here that this expression is a simplification meant for easier writing: the upper term gives the normalization by the electromagnetic energy and should include the contribution of the magnetic energy and of the time averaging. As they are responsible for factors 2 and $\frac{1}{2}$, respectively, which cancels themselves out, this is usual for the definition of the mode volume.

From the quantum theory of coupled resonators based on the Hopfield model presented in the main text, the one photon coupled states $|\pm_1\rangle$ are the result of the hybridization of the one photon uncoupled states $|1_A, 0_B\rangle$ and $|0_A, 1_B\rangle$,

$$\begin{aligned} |+_1\rangle &= \cos\theta|1_A, 0_B\rangle + \sin\theta|0_A, 1_B\rangle, \\ |-_1\rangle &= \sin\theta|1_A, 0_B\rangle - \cos\theta|0_A, 1_B\rangle, \end{aligned} \tag{E3}$$

with θ being defined by $\tan(2\theta) = -\frac{2G}{\delta}$, $\delta = \omega_B - \omega_A$. In order to compute the mode volume of the coupled modes using this expression, we evaluate in the following the quantity $|E(r)|^2$ as $\langle\pm_1|\boldsymbol{E}(r)^2|\pm_1\rangle$, using the electric field operator $\boldsymbol{E} = \boldsymbol{E}_A(r) + \boldsymbol{E}_B(r)$ with

$$\begin{aligned} \boldsymbol{E}_A(r) &= i\mathcal{E}_A(a f_A(r) - a^\dagger f_A^*(r)), \\ \boldsymbol{E}_B(r) &= i\mathcal{E}_B(b f_B(r) - b^\dagger f_B^*(r)), \end{aligned} \tag{E4}$$

where $\mathcal{E}_j = \sqrt{\frac{\hbar\omega_j}{2\epsilon_0 V_j}}$ are the RMS electric field amplitudes associated to vacuum fluctuations in modes $j = A, B$ and V_j is the uncoupled mode volumes defined at the central position r_0.

First, we expand the expression of $\boldsymbol{E}(r)^2$,

$$\begin{aligned} \boldsymbol{E}(r)^2 &= \boldsymbol{E}_A(r)^2 + \boldsymbol{E}_B(r)^2 + 2\boldsymbol{E}_A(r)\boldsymbol{E}_B(r) \\ &= \mathcal{E}_A^2(|f_A(r)|^2(1 + 2a^\dagger a) - f_A(r)^2 aa - f_A^*(r)^2 a^\dagger a^\dagger) \\ &\quad + \mathcal{E}_B^2(|f_B(r)|^2(1 + 2b^\dagger b) - f_B(r)^2 bb - f_B^*(r)^2 b^\dagger b^\dagger) \\ &\quad + 2\mathcal{E}_A\mathcal{E}_B(f_A(r)f_B^*(r)ab^\dagger - f_A(r)f_B(r)ab + \text{h.c.}). \end{aligned}$$

Following the rotating wave approximation, only resonant terms have non-zero contributions to the expectation value $\langle\pm_1|\boldsymbol{E}(r)^2|\pm_1\rangle$. For the $|+_1\rangle$ state,

$$\begin{aligned} &\langle+_1|\boldsymbol{E}(r)^2|+_1\rangle \\ &= 3\cos^2\theta\mathcal{E}_A^2|f_A(r)|^2 + 3\sin^2\theta\mathcal{E}_B^2|f_B(r)|^2 \\ &\quad + 2\sin\theta\cos\theta\mathcal{E}_A\mathcal{E}_B\,\mathrm{Re}(f_A f_B^*). \end{aligned} \tag{E5}$$

Let us now evaluate the up and bottom terms of the expression of the mode volume using this expression. The upper term gives the expression of the matrix element of the Hamiltonian operator for the state $|+_1\rangle$,

$$\begin{aligned} &\int \epsilon(r)\langle+_1|\boldsymbol{E}(r)^2|+_1\rangle \mathrm{d}^3 r \\ &= \frac{3}{2}\cos^2\theta\hbar\omega_A + \frac{3}{2}\sin^2\theta\hbar\omega_B \\ &\quad + 2\sin\theta\cos\theta\sqrt{\frac{\hbar\omega_A\omega_B}{V_A V_B}}\int \epsilon_r(r)\mathrm{Re}(f_A f_B^*)\mathrm{d}^3 r, \end{aligned} \tag{E6}$$

whose value is directly $\frac{3}{2}\hbar\omega_+$ since $|+_1\rangle$ is an eigenstate. The third term of the above expression is an overlap integral yielding the value of the resonator coupling constant G, if the magnetic contribution is additionally taken into account.

Considering the bottom term, using Eq. (E5) evaluated at r_0 and $f_A(r_0) = f_B(r_0) = 1$,

$$\begin{aligned} &\epsilon(r_0)\langle+_1|\boldsymbol{E}(r_0)^2|+_1\rangle \\ &= \frac{3}{2}\cos^2\theta\frac{\hbar\omega_A}{V_A} + \frac{3}{2}\sin^2\theta\frac{\hbar\omega_B}{V_B} \\ &\quad + \sin\theta\cos\theta\sqrt{\frac{\hbar^2\omega_A\omega_B}{V_A V_B}}. \end{aligned} \tag{E7}$$

We can finally propose an expression for the mode volumes V_+ and V_- of the coupled modes in a symmetric form as follows:

$$V_+ = \frac{\omega_+}{\cos^2\theta\frac{\omega_A}{V_A} + \sin^2\theta\frac{\omega_B}{V_B} + \frac{2}{3}\sin\theta\cos\theta\sqrt{\frac{\omega_A\omega_B}{V_A V_B}}}, \tag{E8}$$

$$V_- = \frac{\omega_-}{\sin^2\theta\frac{\omega_A}{V_A} + \cos^2\theta\frac{\omega_B}{V_B} - \frac{2}{3}\sin\theta\cos\theta\sqrt{\frac{\omega_A\omega_B}{V_A V_B}}}, \tag{E9}$$

from which are deduced the expressions of the main text.

Funding. Agence Nationale de la Recherche (ANR-19-CE24-0015, ANR-22-CE09-0018); European Research Council (820133).

Acknowledgment. The authors thank Jean-Francois Lampin and Jean-Michel Gerard for fruitful discussion on the strong coupling regime and cavity.

Disclosures. The authors declare no conflicts of interest.

Data Availability. Data underlying the results presented in this paper are available upon reasonable request.

REFERENCES

1. E. M. Purcell, "Spontaneous emission probabilities at radio frequencies," Phys. Rev. **69**, 681 (1946).
2. A. F. Kockum, A. Miranowicz, S. De Liberato, S. Savasta, and F. Nori, "Ultrastrong coupling between light and matter," Nat. Rev. Phys. **1**, 19–40 (2019).
3. G. Scalari, C. Maissen, D. Turčinková, D. Hagenmüller, S. D. Liberato, C. Ciuti, C. Reichl, D. Schuh, W. Wegscheider, M. Beck, and J. Faist, "Ultrastrong coupling of the cyclotron transition of a 2D electron gas to a THz metamaterial," Science **335**, 1323–1326 (2012).
4. D. Hagenmüller, S. De Liberato, and C. Ciuti, "Ultrastrong coupling between a cavity resonator and the cyclotron transition of a two-dimensional electron gas in the case of an integer filling factor," Phys. Rev. B **81**, 235303 (2010).
5. J. Keller, G. Scalari, S. Cibella, C. Maissen, F. Appugliese, E. Giovine, R. Leoni, M. Beck, and J. Faist, "Few-electron ultrastrong light-matter coupling at 300 GHz with nanogap hybrid LC microcavities," Nano Lett. **17**, 7410–7415 (2017).
6. B. Paulillo, J.-M. Manceau, L. H. Li, A. G. Davies, E. H. Linfield, and R. Colombelli, "Room temperature strong light-matter coupling in three dimensional terahertz meta-atoms," Appl. Phys. Lett. **108**, 101101 (2016).
7. A. Bayer, M. Pozimski, S. Schambeck, D. Schuh, R. Huber, D. Bougeard, and C. Lange, "Terahertz light–matter interaction beyond unity coupling strength," Nano Lett. **17**, 6340–6344 (2017).
8. Y. Todorov and C. Sirtori, "Few-electron ultrastrong light-matter coupling in a quantum LC circuit," Phys. Rev. X **4**, 041031 (2014).
9. M. Jeannin, G. M. Nesurini, S. Suffit, D. Gacemi, A. Vasanelli, L. Li, A. G. Davies, E. Linfield, C. Sirtori, and Y. Todorov, "Ultrastrong light–matter coupling in deeply subwavelength THz LC resonators," ACS Photon. **6**, 1207–1215 (2019).
10. M. Benito and G. Burkard, "Hybrid superconductor-semiconductor systems for quantum technology," Appl. Phys. Lett. **116**, 190502 (2020).
11. S. André, V. Brosco, M. Marthaler, A. Shnirman, and G. Schön, "Few-qubit lasing in circuit QED," Phys. Scr. **T137**, 014016 (2009).
12. A. Cottet, M. C. Dartiailh, M. M. Desjardins, T. Cubaynes, L. C. Contamin, M. Delbecq, J. J. Viennot, L. E. Bruhat, B. Douçot, and T. Kontos, "Cavity QED with hybrid nanocircuits: from atomic-like physics to condensed matter phenomena," J. Phys. Condens. Matter **29**, 433002 (2017).
13. M. Reitz, C. Sommer, and C. Genes, "Cooperative quantum phenomena in light-matter platforms," PRX Quantum **3**, 010201 (2022).
14. S. De Liberato, "Virtual photons in the ground state of a dissipative system," Nat. Commun. **8**, 1465 (2017).
15. N. M. Peraca, A. Baydin, W. Gao, M. Bamba, and J. Kono, "Ultrastrong light–matter coupling in semiconductors," in *Semiconductors and Semimetals*, S. T. Cundiff and M. Kira, eds. (Elsevier, 2020), Vol. **105**, pp. 89–151.
16. Q. Zhang, M. Lou, X. Li, J. L. Reno, W. Pan, J. D. Watson, M. J. Manfra, and J. Kono, "Collective non-perturbative coupling of 2D electrons with high-quality-factor terahertz cavity photons," Nat. Phys. **12**, 1005–1011 (2016).
17. X. Li, M. Bamba, Q. Zhang, S. Fallahi, G. C. Gardner, W. Gao, M. Lou, K. Yoshioka, M. J. Manfra, and J. Kono, "Vacuum Bloch–Siegert shift in Landau polaritons with ultra-high cooperativity," Nat. Photonics **12**, 324–329 (2018).
18. E. Mavrona, S. Rajabali, F. Appugliese, J. Andberger, M. Beck, G. Scalari, and J. Faist, "THz ultrastrong coupling in an engineered Fabry–Perot cavity," ACS Photon. **8**, 2692–2698 (2021).
19. S. Rajabali, S. Markmann, E. Jöchl, M. Beck, C. A. Lehner, W. Wegscheider, J. Faist, and G. Scalari, "An ultrastrongly coupled single terahertz meta-atom," Nat. Commun. **13**, 2528 (2022).
20. F. Meng, M. D. Thomson, B. Klug, D. Čibiraitė, Q. Ul-Islam, and H. G. Roskos, "Nonlocal collective ultrastrong interaction of plasmonic metamaterials and photons in a terahertz photonic crystal cavity," Opt. Express **27**, 24455–24468 (2019).
21. L. Cao, S. Jia, M. D. Thomson, F. Meng, and H. G. Roskos, "Can a terahertz metamaterial sensor be improved by ultra-strong coupling with a high-*Q* photonic resonator?" Opt. Express **30**, 13659–13672 (2022).
22. F. Meng, M. D. Thomson, B. Klug, and H. G. Roskos, "Strong interaction between two photons and a plasmon of a complementary metamaterial in a terahertz dual cavity," Opt. Express **29**, 42420–42434 (2021).
23. M. Jeannin, T. Bonazzi, D. Gacemi, A. Vasanelli, L. Li, A. G. Davies, E. Linfield, C. Sirtori, and Y. Todorov, "Absorption engineering in an ultrasubwavelength quantum system," Nano Lett. **20**, 4430–4436 (2020).
24. C. Symonds, S. Azzini, G. Lheureux, A. Piednoir, J. M. Benoit, A. Lemaitre, P. Senellart, and J. Bellessa, "High quality factor confined Tamm modes," Sci. Rep. **7**, 3859 (2017).
25. A. Kavokin, I. Shelykh, and G. Malpuech, "Optical Tamm states for the fabrication of polariton lasers," Appl. Phys. Lett. **87**, 261105 (2005).
26. S. Messelot, C. Symonds, J. Bellessa, J. Tignon, S. Dhillon, J.-B. Brubach, P. Roy, and J. Mangeney, "Tamm cavity in the terahertz spectral range," ACS Photon. **7**, 2906–2914 (2020).
27. J. Hopfield, "Theory of the contribution of excitons to the complex dielectric constant of crystals," Phys. Rev. **112**, 1555–1567 (1958).
28. H. Haus and W. Huang, "Coupled-mode theory," Proc. IEEE **79**, 1505–1518 (1991).
29. S. Fan, W. Suh, and J. D. Joannopoulos, "Temporal coupled-mode theory for the Fano resonance in optical resonators," J. Opt. Soc. Am. A **20**, 569–572 (2003).
30. H. A. Haus, *Waves and Fields in Optoelectronics* (Prentice-Hall, 1984).
31. M. A. Ordal, R. J. Bell, R. W. Alexander, L. L. Long, and M. R. Querry, "Optical properties of Au, Ni, and Pb at submillimeter wavelengths," Appl. Opt. **26**, 744–752 (1987).
32. C. Sauvan, J.-P. Hugonin, I. S. Maksymov, and P. Lalanne, "Theory of the spontaneous optical emission of nanosize photonic and plasmon resonators," Phys. Rev. Lett. **110**, 237401 (2013).
33. R. Coccioli, M. Boroditsky, K. Kim, Y. Rahmat-Samii, and E. Yablonovitch, "Smallest possible electromagnetic mode volume in a dielectric cavity," IEE Proc. Optoelectron. **145**, 391–397 (1998).
34. S. Messelot, E. Riccardi, S. Massabeau, F. Valmorra, M. Rosticher, K. Watanabe, T. Taniguchi, J. Tignon, T. Boulier, V. Dauvois, M. Delbecq, S. Dhillon, S. Balibar, T. Kontos, and J. Mangeney, "Large terahertz electric dipole of a single graphene quantum dot," Phys. Rev. Res. **4**, L012018 (2022).
35. C. Zhang, J. Wu, B. Jin, Z. Ji, L. Kang, W. Xu, J. Chen, M. Tonouchi, and P. Wu, "Low-loss terahertz metamaterial from superconducting niobium nitride films," Opt. Express **20**, 42–47 (2012).
36. J. Keller, G. Scalari, F. Appugliese, E. Mavrona, S. Rajabali, M. J. Suess, M. Beck, and J. Faist, "High T_c superconducting THz metamaterial for ultrastrong coupling in a magnetic field," ACS Photon. **5**, 3977–3983 (2018).
37. Y. P. Bliokh, J. Felsteiner, and Y. Z. Slutsker, "Total absorption of an electromagnetic wave by an overdense plasma," Phys. Rev. Lett. **95**, 165003 (2005).
38. Z.-Y. Yang, S. Ishii, T. Yokoyama, T. D. Dao, M.-G. Sun, P. S. Pankin, I. V. Timofeev, T. Nagao, and K.-P. Chen, "Narrowband wavelength selective thermal emitters by confined Tamm plasmon polaritons," ACS Photon. **4**, 2212–2219 (2017).
39. C. Maissen, G. Scalari, F. Valmorra, M. Beck, J. Faist, S. Cibella, R. Leoni, C. Reichl, C. Charpentier, and W. Wegscheider, "Ultrastrong coupling in the near field of complementary split-ring resonators," Phys. Rev. B **90**, 205309 (2014).